NANO LETTERS

2001
Vol. 1, No. 12
677−682

Local Energy Transfer in Self-Assembled Polyelectrolyte Thin Films Probed by Near-Field Optics

Geoffrey M. Lowman,[†] Natalie Daoud,[†] Ryan M. Case,[‡] Paul J. Carson,[†] and Steven K. Buratto*,[†]

Department of Chemistry and Biochemistry and Department of Physics, University of California, Santa Barbara, California 93106-9510

Received July 31, 2001; *Revised Manuscript Received September 20, 2001*

ABSTRACT

Near-field scanning optical microscopy (NSOM) has been used to investigate spatially localized energy transfer properties of self-assembled polyelectrolyte films consisting of poly(*p*-phenylene vinylene) (PPV) and poly(allylamine hydrochloride) (PAH) doped with Texas Red dye (TR-PAH). Local differences in energy transfer efficiency highlight the unique multilayer interpenetration properties of thin films constructed using the layer-by-layer (LbL) electrostatic self-assembly technique, as well as the importance of localized probes, to discern local variation that would not be observed using spatially averaged measurements.

Polyelectrolyte layer-by-layer (LbL) self-assembly has become an attractive method for constructing and introducing functionality into thin film architectures. The technique, introduced by Decher,[1−3] is based primarily on electrostatic interaction[4−6] between alternately charged adsorbed polyelectrolyte layers. Since the preliminary development of the technique, many active materials have been incorporated into LbL films, including proteins,[7−10] metal and semiconductor nanoparticles,[11−17] and dye molecules.[18,19] The LbL approach has also been applied to create organic light-emitting diodes (OLEDs),[20−22] to improve interfacial properties in conventional OLEDs,[23] and to create micropatterned arrays.[24,25]

LbL self-assembly forms films with predictable overall thickness, but the internal layer structure is less distinct. Neutron reflectivity studies have demonstrated interlayer mixing that can extend up to 2.5 polycation\polyanion bilayers,[26−29] which has consequences in the bulk material properties of LbL films. Radiationless energy transfer (ET) between chromophores incorporated into specific layers in LbL films has been employed as a complementary optical tool for characterizing this internal layer structure.[30−33] In the model developed by Förster,[34] radiationless ET proceeds by a dipole−dipole interaction with an R^{-6} distance dependence, which leads to a range of distances for ET typically greater than 10 Å and makes it an ideal optical tool for characterizing macromolecular systems. The groundwork for ET experiments in thin films was conducted on Langmuir−Blodgett (LB) films over thirty years ago.[35] These studies also developed the theoretical framework for steady-state ET efficiencies in 2-D systems.[36] The separation of the donor and acceptor layers in a 2-D array shows dependence on the photoluminescence intensity of the donor layer given by

$$\left[\frac{I_d}{I_\infty}\right] = \frac{1}{1 + (d_0/d)^4} \tag{1}$$

In this equation I_d is the photoluminescence intensity of the donor array spaced a distance d from the acceptor array. I_∞ is the photoluminescence intensity of the donor in the absence of the acceptor array, and d_0 is the particular spacing between the donor and acceptor arrays that corresponds to a 50% probability of ET and is given theoretically by

$$d_0{}^4 = \frac{\alpha^4 \Phi_d}{n^4} \int_0^\infty A_\lambda I_\lambda \lambda^4 \, d\lambda \tag{2}$$

where α is an dipole orientation factor, n is the index of refraction of the material between the donor and acceptor arrays, Φ_d is the quantum yield of photoluminescence for the donor array. The integral in eq 2 is the spectral overlap between the donor photoluminescence intensity (I_λ) and the acceptor absorbance (A_λ) as a function of the wavelength.

Energy transfer efficiency was calculated using the intensity of the fluorescence from the combination of the donor and acceptor, taken from a fit of the fluorescence spectra, rather than simply calculating the dependence of the fluorescence intensity of the donor or acceptor separately.

* Corresponding author e-mail: buratto@chem.ucsb.edu.
[†] Department of Chemistry and Biochemistry.
[‡] Department of Physics.

10.1021/nl0155936 CCC: $20.00
Published on Web 10/06/2001

The major problem in fitting spectra exhibiting ET is the overlap of the donor and acceptor emission. We chose to use a reference fluorescence spectrum of PPV without the presence of an acceptor as a basis for fitting the donor portion of the ET spectra. Examples of fits resulting from this procedure are shown in red in Figures 3 and 4, with individual Gaussians shown in gray. The integrated areas under the respective Gaussian curves were used to calculate the fluorescence intensity for the donor and the acceptor. The values for fluorescence intensity were used to calculate ET efficiency (χ) according to the following equation:

$$\chi = \frac{1}{1 + \frac{\xi_2 I_1}{\xi_1 I_2}} \tag{3}$$

where ξ_1 and ξ_2 are the quantum efficiency for the donor (PPV = 0.15) and the acceptor (Texas Red = 0.90).[41] I_1 and I_2 are the fluorescence intensity of the donor and acceptor, respectively, and are given by

$$I_1 = (1 - \chi)\xi_1 I_0 \tag{4}$$

$$I_2 = \chi \xi_2 I_0 \tag{5}$$

where I_0 is the excitation intensity.

Previous studies of ET in LbL films have depended on fluorescence or absorbance measurements that are spatially averaged over large areas of the film to calculate ET efficiencies, in essence treating the LbL film as discreet 2-D layers and combining theoretical models to determine the amount of intermixing of the layers.[32,33] The work reported here adds a new dimension to measuring ET in LbL films. Using the scan probe microscopy method of near-field scanning optical microscopy (NSOM), ET efficiencies can be calculated from fluorescence spectra taken from localized regions in a particular film, and a more direct measurement of intermixing can be made. Polyelectrolyte films require that properties defined on the nanoscale in an individual layer extend to the macroscale. This technique allows regions of high and low ET efficiency to be identified with precision on the order of the diameter of the aperture of the NSOM probe (normally 100−125 nm). NSOM has the added advantage of providing information on both the nanoscale morphology and fluorescence properties of the film simultaneously. An additional feature of this NSOM study is that by combining several local ET measurements we can calculate an averaged ET efficiency, which can be compared to those calculated from spatially averaged techniques. It should be noted that NSOM has been applied to measure ET in an LbL multilayer film previously.[31] The self-assembled system studied in ref 31 incorporated α-zirconium phosphate layers that drastically change the intermixing properties of the polyelectrolyte layer compared to a film that is made solely of polyelectrolytes, but the study outlined the importance of high-resolution measurement of energy transfer for use in describing the morphologies and photophysical properties of multilayer systems on the nanoscale.

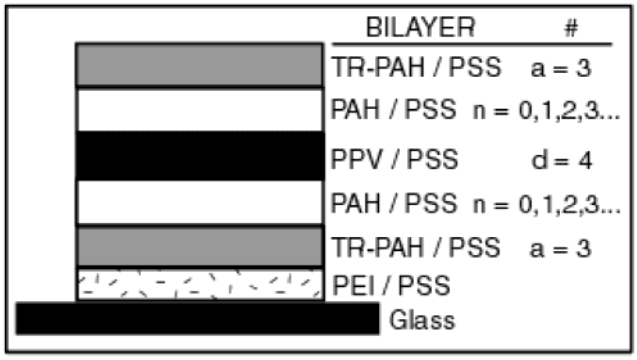

Figure 1. Schematic of polyelectrolyte LbL film structure. The four donor bilayers (d), shown in black, are constructed between two groups of three acceptor bilayers (a), shown in gray, with various separation distances set by the number of optically inactive bilayers (n), shown in white.

Specifically, this study marked the first time spatially resolved fluorescence ET was used as a tool for discerning order in multilayer assemblies. We present NSOM measurements of local ET in an LbL film consisting of poly(*p*-phenylene vinylene) (PPV) and poly(allylamine hydrochloride) (PAH) doped with Texas Red (sulforhodamine 101 acid chloride) (TR-PAH) as donor and acceptor layers, respectively. The Texas Red acceptor chromophore is not efficiently excited at the wavelength (457 nm) used to excite the PPV donor layers. We observe differences in ET efficiency in localized regions of LbL films, as well as tracking the average ET efficiency as the donor and acceptor layers are separated by varying the thickness of optically inactive polycation layers of PAH and polyanion layers of poly(styrene sulfonate) (PSS).

Film Preparation. Polyelectrolyte LbL films were prepared on microscope cover glass (Fisher, size 25 × 25 × 0.5 mm^3) which was cleaned by immersion in piranha solution H_2SO_4/H_2O_2 (7:3 by volume) and RCA solution $H_2O/H_2O_2/NH_4OH$ (5:1:1 by volume). Ultra-purified (Millipore) water (pH = 5.5) was used for all preparation steps. Texas Red and PAH were purchased from Aldrich. The procedure for labeling PAH with Texas Red dye has been described elsewhere.[31] PSS was purchased from Acros Organics. Poly(ethyleneimine) (PEI) was purchased from Polysciences Inc. A priming layer of PEI (0.01 M with respect to the monomer MW) was used on all films described in this study. The PEI, PAH, PSS, and TR-PAH layers were all adsorbed from exposure to 0.01 M solutions for 15 min. The water soluble precursor PPV (poly(*p*-xylylene-α-tetrahydrothiophenium) was adsorbed from exposure to a 0.5 mg/mL solution for 15 min. No ionic salts were added to the polyelectrolyte solutions during deposition. All adsorption steps were followed by a rinse step using Ultrapure water. Samples containing the precursor PPV were converted to PPV in a vacuum oven at greater than 125 °C and a pressure of 10^{-6} bar.

The LbL film architecture is illustrated in Figure 1. The primary PEI/PSS bilayer was followed by adsorption of three TR-PAH/PSS bilayers. Four PPV/PSS bilayers were adsorbed at a distance from the TR-PAH set by the number

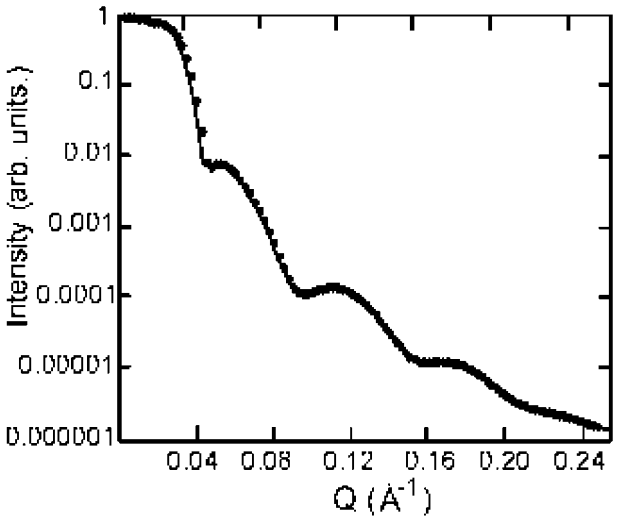

Figure 2. Example of X-ray scattering data of a sample with film architecture: Si/PEI/PSS/(PAH/PSS)$_{11}$. The circles represent the scattering data and the solid line represents a fit to the data. The total film thickness calculated from the fit of this curve was 106 Å, resulting in an average spacer thickness of 8.8 Å.

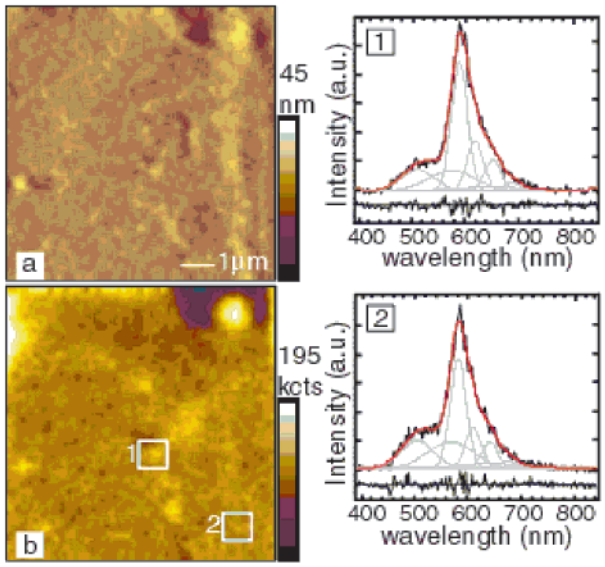

Figure 3. Near-field scanning optical microscopy data from a sample with one spacer bilayer ($n = 1$) between donor and acceptor layers. A strong correlation is shown between the topography (a) and fluorescence (b) images. Local spectra (10 s integration) were collected in the areas marked in the fluorescence image. The spectra (1,2) are shown with a combined fit to the donor and acceptor contribution (red line), and the residual to the fit. Calculated energy transfer efficiencies (χ) for spectra 1 and 2 were 0.31 and 0.22, respectively.

(n) of optically inactive PAH/PSS bilayers. After construction the PPV/PSS bilayers, we repeated the assembly of an equal number of spacer PAH/PSS bilayer(s) and three bilayers of TR-PAH. It should be noted that at $n = 0$ there remains a PSS layer separating the PPV and TR-PAH optically active layers.

Small-angle X-ray scattering (SAXS) film thickness measurements were made using a custom built 4-circle X-ray diffractometer with a scintillation detector (Bicron) and a Rigaku 18 kW X-ray generator. All LbL film samples used for thickness determination were assembled on silicon wafer substrates from the same polyelectrolyte solutions as the samples used in optical studies. Silicon substrates were cleaned in a 1:1 solution of hydrochloric acid and methanol for 1 h, followed by an extensive rinse in Ultrapure water. Film samples with the architecture Si/PEI/PSS/(PAH/PSS)$_{11}$ were constructed in order to determine the thickness of the optically inactive spacer layers. Films studied with SAXS yielded typical Kiessig oscillations from constructive and deconstructive interference from reflectivity from the air/film and film/substrate interfaces. The thickness of the film can subsequently be derived from the positions of the maxima and minima of the oscillations in the reflectivity curve. All samples used in thickness measurements were exposed to the same heating procedure used to facilitate the elimination reaction to form PPV, as this procedure can decrease water content in the film and lead to a decrease in thickness. The average spacer bilayer thickness determined from this procedure was 8.8 Å, with an average calculated surface roughness of 0.5 Å per bilayer.

Near-Field Optical Microscopy. The NSOM/shear force apparatus used for this study has been described in detail elsewhere.[37] Near-field excitation is accomplished using a subwavelength aperture that exists at the end of a tapered optical fiber coated with 100 nm of Ag.[38] The tapered fibers are fabricated using a commercial pipet puller with a 10 W CO_2 laser as the heat source. Metallization of the fiber tips is done by thermal evaporation at a base pressure of 2×10^{-6} Torr with the tips positioned at a slight angle to shadow the end from the metal source. All of the tips used in this study are optimized for throughput of the excitation wavelength, 457 nm from an Ar^+ laser, and yield a maximum illumination power of 1 kW/cm^2.

The standard optically detected shear force technique,[39,40] an analogue to attractive mode atomic force microscopy (AFM), is used to maintain the tip within the near-field (~10 nm) of the surface of the sample. This feedback mechanism also provides an independent topography image of the surface by raster scanning the sample while keeping the tip fixed. Rastering of the sample is controlled by commercial scanning probe microscopy electronics (Digital Instruments, Santa Barbara, CA).

The fluorescence signal from the spot illuminated by the NSOM probe is collected with a high numerical aperture (N. A. = 0.85) objective and routed to either an avalanche photodiode (APD) (EG&G, Canada) for imaging or to a spectrometer/CCD (Princeton Instruments) for local spectroscopy via the optics of a conventional optical microscope. The excitation wavelength is suppressed using a holographic notch filter.

A collection of NSOM data from a sample described in Figure 1 with one spacer layer ($n = 1$) is shown in Figure 3. We observe a strong correlation between elevated features in the topography image (Figure 3a) and more intense features in the fluorescence image collected over the entire visible region (Figure 3b), but it cannot be determined from the images alone whether the increase in fluorescence

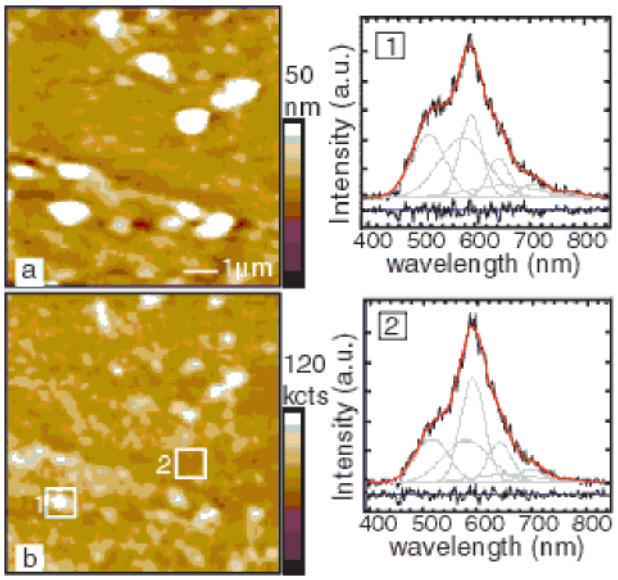

Figure 4. Near-field scanning optical microscopy data from a sample with two spacer bilayers ($n = 2$) between donor and acceptor layers. Local spectra (10 s integration) were collected in the areas marked in the fluorescence image. The spectra (1,2) are shown with a combined fit to the donor and acceptor contribution (red line), and the residual to the fit. Calculated energy transfer efficiencies (χ) for spectra 1 and 2 were 0.13 and 0.18, respectively.

intensity rises from the donor or acceptor emission. The NSOM technique affords the capability to position the excitation source in very precise localized regions of the film in order to collect fluorescence spectra. The spectra shown in Figure 3 were collected from a feature near the middle of the image in Figure 3b and the ridge on the right side of the image in Figure 3b as marked. One concern in working with PPV in ambient atmosphere is the threat of photooxidation. We typically see the effects of photooxidation after roughly 30−60 s of illumination, depending on excitation power. To minimize photooxidation the following procedure was used to collect localized spectra. (1) The topography image was collected without laser excitation. (2) The excitation source was positioned on various locations illustrated by the topography image, the sample was illuminated by the probe source, and fluorescence spectra were collected. Thermal drift of the probe tip is negligible in comparison to the topographical features found in the films investigated in this study. (3) Finally, the sample was scanned again, with laser excitation, to collect a topography and fluorescence image simultaneously. We observe no discernible signature of photooxidation in the fluorescence image (Figure 3b) or the spectra shown in Figure 3.

A second collection of NSOM data from a sample described in Figure 1 with two spacer layers ($n = 2$) is shown in Figure 4. Again, we observe a strong correlation between elevated features in the topography image (Figure 4a) and more intense features in the fluorescence image (Figure 4b). The spectra shown in Figure 4 were collected from an area of raised topography and intense fluorescence intensity (Figure 4 spectrum 1) and an area of decreased fluorescence intensity (Figure 4 spectrum 2).

The spectra shown in Figures 3 and 4 exhibit a characteristic line shape attributed to ET between PPV and TR-PAH. The PPV donor emission that is not quenched by ET to the acceptor falls in the range of 450−500 nm. From 550 to 700 nm the spectra in Figures 3 and 4 are dominated by emission from the acceptor. Although the spectra shown in Figure 3 were collected within 3 μm separation, we observe a large difference in ET efficiency shown most distinctly by the relative increase in donor (PPV) fluorescence intensity (shown by the peak centered at 525 nm). The spectra shown in Figure 4 show a more distinct increase in donor fluorescence intensity than those shown in Figure 3, but in this case it appears that the increased intensity in the fluorescence image (Figure 4b) can be attributed to increased fluorescence from the donor.

To discern the uniformity of emission from a scanned region of film we, collected NSOM fluorescence images in two spectral regions. Monitoring the fluorescence of a particular spectral region during NSOM data acquisition will allow the contribution of each of the donor and acceptor emission to be imaged directly. The spectral regions of the donor and acceptor emission were separated with band-pass filters inserted just prior to the APD detector, <550 nm (primarily donor emission) and >570 nm (primarily acceptor emission). A representative collection of data from these experiments is shown in Figure 5. The topography image in Figure 5a shows several elevated features of a film with two PAH/PSS spacer layers ($n = 2$). The fluorescence images shown in Figures 5b,c were collected in spectral regions >570 nm and <550, respectively. The emission from the TR-PAH acceptor layers (Figure 5b) shows strong correlation between regions of increased fluorescence intensity and areas of elevated topography in Figure 5a. It should be noted that the darker areas in Figure 3b show only relatively lower fluorescence intensity and not lack of fluorescence. This correlation suggests that the increased emission from the acceptor layers in some regions can be attributed to local thickness differences and is not direct evidence for aggregation of the dye molecules in the film. These thickness differences are most likely the largest cause for the difference in ET efficiency between local regions of the same sample. In comparison, the emission collected from the spectral region of the donor (Figure 5c) shows more uniform emission. With the exception of the two regions pointed out in Figure 5b,c, the areas of increased fluorescence intensity in the donor emission are not correlated with increased emission of the acceptor (indicating ET). The regions indicated with arrows in Figure 5c show strong emission in both donor and acceptor spectral regions and show energy being transferred to the acceptor, but at this separation distance ($n = 2$) show a significant amount of emission directly from the donor layers.

A distribution of spectra collected from samples containing spacer $(PAH/PSS)_n$ bilayers with $n = 0, 1, 2, 3$ is shown in Figure 6a. The spectra in Figure 6a clearly illustrate the decrease in acceptor emission and increase in donor emission as the distance between the donor and acceptor layers increases. The increase in donor emission at large separation

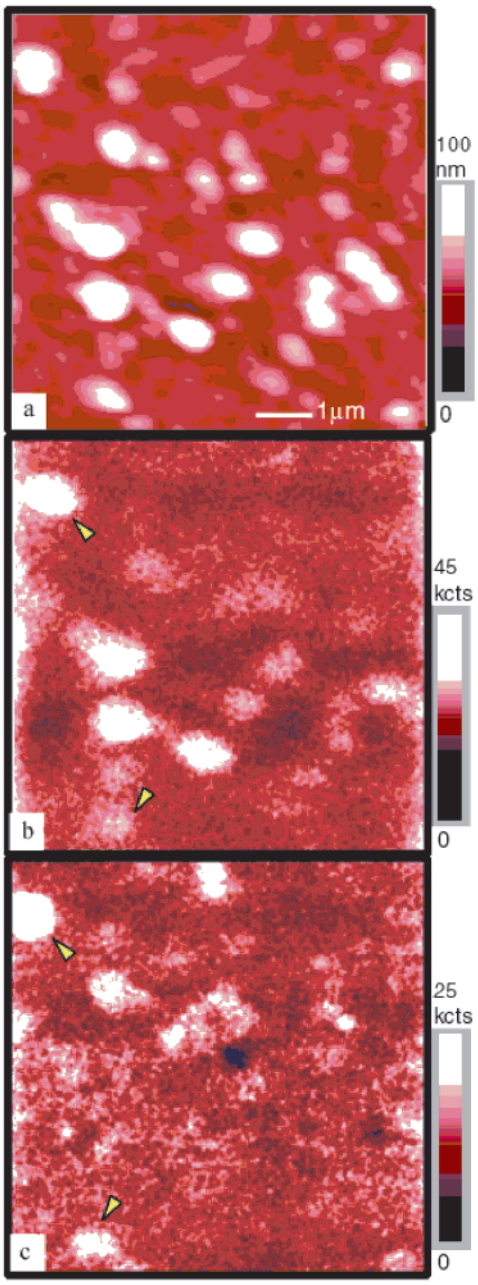

Figure 5. NSOM topography (a) and fluorescence images from the spectral region of the acceptor (b) and donor (c). Image b corresponds to emission >570 nm and image c corresponds to emission <550 nm. Arrows indicate areas of strong emission in both the donor and acceptor spectral regions.

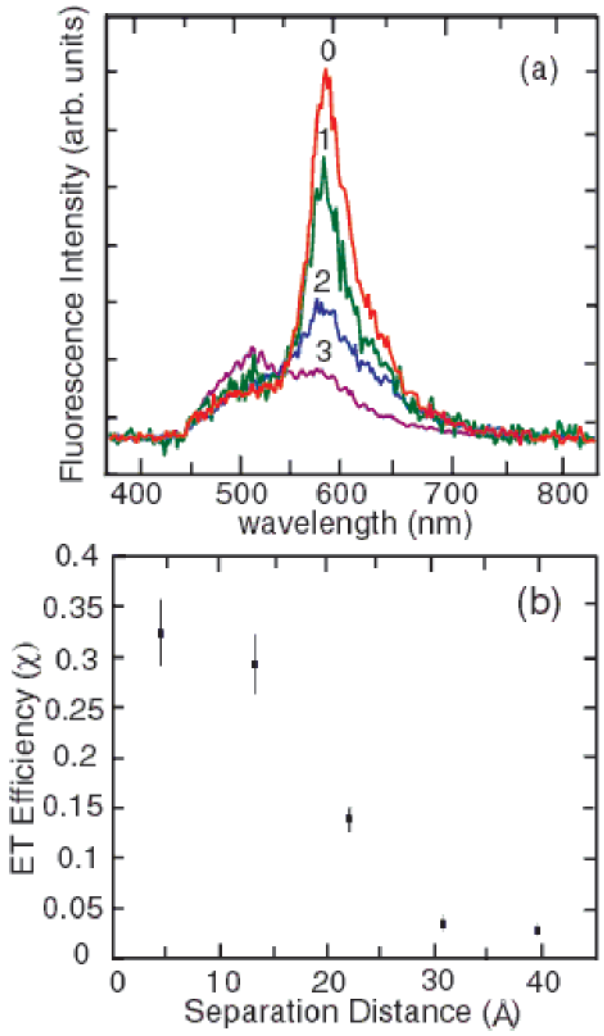

Figure 6. (a) Fluorescence spectra of films with different donor/acceptor spacing as denoted by the number of spacer bilayers shown above each spectrum. The distinct drop in acceptor fluorescence intensity (550−700 nm) and rise in donor fluorescence intensity (450−500 nm) is indicative of energy transfer between the chromophores. The energy transfer efficiencies (χ) calculated from the spectra shown are 0.361 for $n = 0$, 0.238 for $n = 1$, 0.084 for $n = 2$, and 0.007 for $n = 3$. (b) Calculated average energy transfer efficiencies (χ) as a function of donor/acceptor spacing as measured by small-angle X-ray scattering. The bars on each data point correspond to the standard deviation of the efficiency values at each separation distance.

distance is less distinct than the decrease in acceptor emission due to the large difference in quantum efficiency of the two chromophores (PPV = 0.20, TR = 0.90). The spectra shown in Figure 6a were normalized to the excitation intensity.

After a number of local spectra from a particular sample are collected and ET efficiency is calculated for each, an average efficiency can be calculated for a particular spacing between donor and acceptor. This leads to a value for ET efficiency that would correspond to that calculated from a measurement using spatially averaged techniques. Figure 6b shows average energy transfer efficiency values at various separation distances. A decrease in ET efficiency with separation distance is observed, as would be expected from two-dimensional ET theory. The standard deviation from the average energy transfer efficiency values is also shown in Figure 6b. The values for the standard deviation are substantial (nearly 20% of the value for $n = 0, 1$) and show the importance of using spatially resolved techniques for measurement of fluorescence properties in polyelectrolyte multilayer films. Using the relationship between average ET efficiencies and separation distance, we can estimate a distance of interpenetration of the active layer through the spacer layers in the areas where local spectra were taken and ET efficiency was calculated. As an example, the energy transfer efficiencies from the spectra shown in Figure 3 correspond to a difference in separation of the active layers

of nearly 12 Å (ET efficiency range of 0.31 to 0.22), or roughly 1.5 spacer bilayers. The difference between these measurements of energy transfer would have been convoluted using spatially averaged techniques to record fluorescence intensity.

NSOM has been used as both a spatially and spectrally localized probe of energy transfer within self-assembled polyelectrolyte thin films. Energy transfer is one route to discern the level of interpenetration between successive layers. We show that the ability to make localized spectroscopic measurements yields information that would be lost using spatially averaged methods. These high-resolution measurements show that energy transfer can be used to demonstrate that LbL films self-assemble in expected structures, and further that locally measured ET efficiencies can be used to describe interpenetration properties in regions of LbL films on the scale of the NSOM probe tip diameter. Further experiments will involve testing other polyelectrolyte systems using this technique, as well as incorporating barriers to interpenetration such as clay sheets or monolayers of nanocrystals. We also plan to study the effect a new spin coating LbL film growth method[42] has on interpenetration properties of films containing various functional layers.

Acknowledgment. We acknowledge Jim Ji and Jeffery Coffer (Texas Christian University) for synthesis of the precursor PPV. We also acknowledge Roger Pynn for useful discussions regarding the SAXS data. This work was supported by the David and Lucille Packard Foundation, the NSF Nanotechnology Initiative, and the Alfred P. Sloan Foundation.

References

(1) Decher, G.; Hong, J. D. *Makromol. Chem., Macromol. Symp.* **1991**, *46*, 321.
(2) Decher, G.; Hong, J. D.; Schmitt, J. *Thin Solid Films* **1992**, *210/211*, 831.
(3) Decher, G. *Science* **1997**, *277*, 1232.
(4) Schlenoff, J. B.; Ly, H.; Li, M. *J. Am. Chem. Soc.* **1998**, *120*, 7626.
(5) Hoogeveen, N.; Cohen Stuart, M. A.; Fleer, G. J., Böhmer, M. R. *Langmuir* **1996**, *12*, 3675.
(6) Ladam, G.; Schaad, P.; Voegel, J. C.; Schaaf, P.; Decher, G.; Cuisinier, F. *Langmuir* **2000**, *16*, 1249.
(7) Sukhorukov, G. B.; Möhwald, H.; Decher, G.; Lvov, Y. M. *Thin Solid Films* **1996**, *284/285*, 220.
(8) Cassier, T.; Lowack, K.; Decher, G. *Supramol. Sci.* **1998**, *5*, 309.
(9) Ladam, G.; Gergely, C.; Senger, B.; Decher, G.; Voegel, J.-C.; Schaaf, P.; Cuisinier, F. J. G. *Biomacromolecules* **2000**, *1*, 674.
(10) Ladam, G.; Schaaf, P.; Cuisinier, F. J. G.; Decher, G.; Voegel, J.-C. *Langmuir* **2001**, *17*, 878.
(11) Schmitt, J.; Decher, G.; Dressick, W. J.; Brandow, S. L.; Geer, R. E.; Shashidhar, R.; Calvert, J. M. *Adv. Mater.* **1997**, *9*, 61.
(12) Caruso, F.; Lichtenfeld, H.; Giersig, M.; Möhwald, H. *J. Am. Chem. Soc.* **1998**, *120*, 8523.
(13) Gao, M.; Richter, B.; Kirstein, S.; Möhwald, H. *J. Phys. Chem. B* **1998**, *102*, 4096.
(14) Chen, K. M.; Jiang, X.; Kimerling, L. C.; Hammond, P. T. *Langmuir* **2000**, *16*, 7825.
(15) Mamedov, A. A.; Kotov, N. A. *Langmuir* **2000**, *16*, 5530.
(16) Gao, M.; Lesser, C.; Kirstein, S.; Möhwald, H.; Rogach, A. L.; Weller, H. *J. Appl. Phys.* **2000**, *87*, 2297.
(17) Joly, S.; Kane, R.; Radzilowski, L.; Wang, T.; Wu, A.; Cohen, R. E.; Thomas, E. L.; Rubner, M. F. *Langmuir* **2000**, *16*, 1354.
(18) Ariga, K.; Lvov, Y.; Kunitake, T. *J. Am. Chem. Soc.* **1997**, *119*, 2224.
(19) Yoo, D.; Wu, A.; Lee, J.; Rubner, M. F. *Synth. Met.* **1997**, *85*, 1425.
(20) Fou, A. C.; Onitsuka, O.; Ferreira, M.; Rubner, M. F. *J. Appl. Phys.* **1996**, *79*, 7501.
(21) Onitsuka, O.; Fou, A. C.; Ferreira, M.; Hsieh, B. R.; Rubner, M. F. *J. Appl. Phys.* **1996**, *80*, 4067.
(22) Ho, P. K. H.; Granström, M.; Friend, R. H.; Greenham, N. C. *Adv. Mater.* **1998**, *10*, 769.
(23) Ho, P. K. H.; Kim, J.-S.; Burroughes, J. H.; Becker, H.; Li, S. F. Y.; Brown, T. M.; Cacialli, R.; Friend, R. H. *Nature* **2000**, *404*, 481.
(24) Clark, S. L.; Hammond, P. T. *Adv. Mater.* **1998**, *10*, 1515.
(25) Hammond, P. T. *Curr. Opin. Colloid Interface Sci.* **2000**, *4*, 430.
(26) Lösche, M.; Schmitt, J.; Decher, G.; Bouwman, W. G.; Kjaer, K. *Macromolecules* **1998**, *31*, 8893.
(27) Tarabia, M.; Hong, H.; Davidov, D.; Kirstein, S.; Steitz, R.; Neumann, R.; Avny, Y. *J. Appl. Phys.* **1998**, *83*, 725.
(28) Kellog, G. J.; Mayes, A. M.; Stockton, W. B.; Ferreira, M.; Rubner, M. F. *Langmuir* **1996**, *12*, 5109.
(29) Schmitt, J.; Grunewald, T.; Decher, G.; Pershan, P. S.; Kjaer, K.; Losche, M. *Macromolecules* **1993**, *26*, 7058.
(30) Kaschak, D. M.; Mallouk, T. E. *J. Am. Chem. Soc.* **1996**, *118*, 4222.
(31) Kerimo, J.; Adams, D. M.; Barbara, P. F.; Kaschak, D. M.; Mallouk, T. E. *J. Phys. Chem. B* **1998**, *102*, 9451.
(32) Richter, B.; Kirstein, S. *J. Chem. Phys.* **1999**, *111*, 5191.
(33) Baur, J. W.; Rubner, M. F.; Reynolds, J. R.; Kim, S. *Langmuir* **1999**, *15*, 6460.
(34) Förster, T. *Ann. Phsyk.* **1948**, *2*, 55.
(35) Kuhn, V. H.; Möbius, D. *Angew. Chem.* **1971**, *83*, 672.
(36) Kuhn, H. *J. Chem. Phys.* **1970**, *53*, 101.
(37) Weston, K. D.; DeAro, J. A.; Buratto, S. K. *Rev. Sci. Instrum.* **1996**, *67*, 2924.
(38) Betzig, E.; Trautman, J. K.; Harris, T. D.; Weiner, J. S.; Kostelak, R. L. *Science* **1991**, *251*, 1468.
(39) Betzig, E.; Finn, P. L.; Weiner, J. S. *Appl. Phys. Lett.* **1992**, *60*, 2484.
(40) Toledo-Crow, R.; Yang, P. C.; Chen, Y.; Vaeziravani, M. *Appl. Phys. Lett.* **1992**, *60*, 2957.
(41) Molecular Probes homepage. http://www.molecularprobes.com (accessed April 2001).
(42) Lee, S. S.; Hong, J. D.; Kim, C. H.; Kim, K.; Koo, J. P.; Lee, K. B. *J. Phys. Chem. B* **2001**, *34*, 5358.

NL0155936